JOURNAL OF AIRCRAFT
Vol. 46, No. 6, November–December 2009

Design and Testing of a Fiber-Metal-Laminate Bird-Strike-Resistant Leading Edge

Michele Guida,* Francesco Marulo,† and Tiziano Polito*
University of Naples "Federico II," 80125 Naples, Italy
Michele Meo‡
University of Bath, Bath, England BA2 7AY, United Kingdom
and
Massimo Riccio§
Alenia Aeronautica, 80058 Pomigliano d'Arco, Naples, Italy

DOI: 10.2514/1.43943

One of the major concerns related to flight safety is the impact of birds. To minimize the risks, there is the need to improve impact resistance of aircraft by developing high-performance materials and better structural design of aircraft structures. Because of their remarkable impact properties, fiber metal laminates with layers of aluminum alloy and high-strength glass-fiber composite are potential candidate materials to be employed for aircraft structures susceptible to bird strikes. This paper describes an experimental and numerical campaign aimed at assessing the bird strike resistance of a fiber-metal-laminate–composite leading edge for the wing of a transport aircraft. Three different fiber-metal-laminate leading-edge structures were designed using advanced finite element simulations; they were manufactured and finally tested to analyze their impact-energy-absorbing capabilities. The finite element models were developed, adopting a Lagrangian approach in such a way to be able to correctly simulate impacts with large deformations and perforations of the structures and to characterize the different inelastic/brittle behaviors and failure modes of the fiber metal laminates. The numerical simulations were generally in good agreement with the experimental values, demonstrating the robustness of the developed finite element simulations in supporting the design of bird-strike-resistant aircraft structures.

Nomenclature

A, B, C, n, and m = parameters in the Johnson–Cook constitutive relation
D = diameter, mm
E = Young's modulus in the direction of x, GPa
G = in-plane shear modulus, GPa
l = length of each of the cell faces, mm
S = failure stress in the pane shear, MPa
T = weighting factor
T_r, T_{melt} = room and melting temperature, °C
t = time, s
th = thickness of an individual sheet, mm
υ = Poisson's coefficient
X_c = fiber compressive failure stress in a large structural direction, MPa
X_T = fiber tensile failure stress in a large structural direction, MPa
Y_C = fiber compressive failure stress in a lateral structural direction, MPa
Y_T = fiber tensile failure stress in a lateral structural direction, MPa
γ = effective plastic shear strain, MPa
ε = strain, mm/mm
$\dot{\varepsilon}$ = effective strain rate, s^{-1}
ε_D = densification strain, mm/mm
ε_p = effective plastic strain, mm/mm
ε_r = deformation at failure, mm/mm
$\dot{\varepsilon}_0$ = reference strain rate, s^{-1}
θ = angle of the honeycomb's cell wall, deg
ρ = mass density, kg/m^3
σ = stress, MPa
σ_r = rupture stress, MPa
σ_y = static yield stress, MPa
τ = shear stress, MPa
τ_L = shear stress in the direction L, MPa
τ_W = shear stress in the direction W, MPa

I. Introduction

BIRD strikes have been a concern to both civil and military aircraft. The external surfaces of an aircraft [which include the nacelles, canopies, wind leading edge (LE), engines, etc.] are susceptible to bird strikes. Aircraft LEs must be designed to absorb impact energy in order to protect the primary structures in the event of bird strike. It is therefore critical to ensure that the aircraft LEs are able to withstand such high velocity impact to guarantee the safe landing of the aircraft after the strike. Currently, commercial aircraft are capable of operating at a high speed greater than 250 kt and at an altitude of 10,000 ft above ground level. Current design, construction, and certification standards (CS) for these aircraft were developed over 40 years ago. Moreover, the population development of large flocking birds has increased dramatically in many parts of the world. Many researchers focused their scientific research on this problem, and most aeronautical companies built new airplanes according to these requirements even though neither the design/construction standards nor the operational practices had changed to reflect the new threat due to possible bird strike. The U.S. Federal Aviation Administration (FAA) and the European Aviation Safety Agency (EASA) regulations each amended sections 25.631 [1,2] that states

---

Received 20 February 2009; revision received 13 May 2009; accepted for publication 23 June 2009.

*Ph.D. Researcher, Department of Aerospace Engineering, Via Claudio 21. Member AIAA.

†Professor, Department of Aerospace Engineering, Via Claudio 21. Senior Member AIAA.

‡Lecturer, Department of Mechanical Engineering, Material Research Center. Member AIAA.

§Senior Engineer, Department of Stress Analysis, Viale dell'Aeronautica.

> The empennage structure must be designed to assure capability of continued safe flight and landing of the airplane after impact with an 8 lb bird when the velocity of the airplane (relative to the bird along the airplane's flight path) is equal to V_C (cruise velocity) at sea level, selected under section 25.335(a) [3]. Compliance with this section by provision of redundant structure and protected location of control system elements or protective devices such as splitter plates or energy-absorbing material is acceptable. Where compliance is shown by analysis, tests, or both, use of data on airplanes having similar structural design are acceptable.

Before certification, an aircraft must demonstrate the ability to land safely after being struck by a bird with a reasonable weight anywhere on the structure at normal operating speeds, as specified by FAA section 25.571 [4]. Impacted components must maintain structural integrity during the large transient loading resulting from bird strike loads. Past experience has demonstrated this compliance through an expensive full-scale test. Therefore, there is the desire to improve the modeling capabilities and enable verification by simulation; the explicit finite element (FE) codes have been used to develop high efficiency bird-proof structures. These codes adopted various FE methods to model the impact phenomena: the Lagrangian approach, the techniques based on Eulerian or arbitrary Lagrangian–Eulerian (ALE) approach, and (recently) the solvers based on the smoothed particle hydrodynamics (SPH) method.

This work is the result of a collaborative research project between a university (the University of Naples "Federico II") and an industrial partner (Alenia Aeronautica) to design a new wing LE composite structure using FE analysis. Extensive experience has been gained with metallic LEs subjected to bird strike [5,6]. However, very limited data exist for composite or hybrid metal/composite structures. In this work, three different configurations have been used to correlate the results; the materials considered are the same, but two different thicknesses about the outboard skin are used for the bird strike analysis.

The wing LE structure is the assembly of three different plies. In this work, we distinguish the ply of the outboard skin as a glass-based fiber metal laminate (FML), the ply of the core skin as honeycomb, and the ply of the inboard skin as an aluminum alloy. This configuration was designed, built, and subjected to bird strike tests. Similarly, FE models help the simulation of the bird strike tests. FML are a family of materials consisting of alternating plies of thin aluminum alloy and fiber/epoxy. The concept of FML originated at Fokker in the Netherlands in the 1950s, and extensive development work has been performed since the 1970s [7]. The laminates can be formed and machined like aluminum alloys and have a high specific strength similar to composite materials. Another major advantage of the laminates is impact strength; during this research project, we carried out an extensive test programmed on the impact resistance of FML. Static, low-velocity (up to 17.5 m/s), and impact tests on square plates with a hemispherical steel indenter were performed [8]. We found that glass-fiber-based FML possessed excellent impact resistance, equal or superior to (depending on the layup) monolithic aluminum alloys. Moreover, that impact resistance improved at higher strain rates; for example, the minimum energy to initiate penetration for one particular FML layup was superior to that of a nonclad 2024-T3 aluminum alloy by a factor of almost two. This impact performance of glass-fiber FML is attributed to a favorable high-strain-rate strengthening phenomenon, which occurs in the glass fibers, combined with a relatively high failure strain [9]. The sandwich structure consists of a honeycomb core between a metallic and a laminated composite face plate. The significant mechanisms of energy absorption of these structures are the localized crushing of the core and the bending and stretching of the facings, and energy may be effectively absorbed through both local crushing and global deflection of the structural element as a whole. To construct suitable crashworthy sandwich elements, it is necessary to use components that have a high degree of energy absorption capability and examine the individual and coupled properties of the ingredients (facings and cores) comprising these elements. The core of a sandwich material must possess increased strength in shear to avoid relative sliding of the face plates when a bending deformation is applied on the sandwich panel, then it must be stiff enough to ensure flatness and prevent wrinkling of the intact portions of facings during the whole crushing process.

A detailed FE model was built using the commercial explicit integration code MSC.Dytran [10]. The simulations included the LE and the structure supporting the test article. The final numerical and experimental correlation showed that good correlation was achieved in terms of global structural behavior of the test article, confirming the validity of this approach. In particular, the model was accurate to predict the final deformed shape of the LE and the absence of foreign object penetration, showing that the designed LE made with FML material was able to protect the inner LE structure from damage, thus satisfying the certification requirements.

II. Experimental Setup

Tests were conducted using an air pressure gun that was able to shoot dummy birds at the desired speed, according to the technical specification [11]. The gun consisted of different components.One component was a pressure tank that was able to speed a 3.6 kg bird up to 140 m/s, had a volume of 0.849 m^3, and had a maximum pressure of 1.025 MPa. The other component was the release mechanism that included a cutter, a diaphragm, and a shooting solenoid to allow the instantaneous introduction of gas inside the launching tube and to push the bird. The launching tube was 12 m in length and used to point the shoot. The sabot stripper was optional. In detail, with this apparatus, it was possible to measure the bird weight with an accuracy of 1.8 g, measure the gun angle direction with an accuracy of 0.25 deg, measure the environment temperature with an accuracy of ±2.8°C, and measure the humidity with an accuracy of around 2%. High-speed cameras were used to record the development of the high-speed impact.

The test backup structure layout is shown in Fig. 1. It shows the structure attached to a solid steel rectangular support frame via two interface beams. The support frame is suspended by means of six load cells for measuring the transmitted load in three coordinate directions. The first test was carried out by using some sensors and preparing the test article with accelerometers, a strain gauge, etc. These sensors recorded some acceptable results due to the small dimensions of the test article. In fact, the strike involved all of the structure, and sensors were damaged in the impact, and so the sensors were not considered in the other tests. Figure 1 also shows the target where the impact strikes the one bay of the LE.

The velocity of the projectile is measured by two photocells mounted between the muzzle and the sabot separator. The data acquisition system is a typical high-speed system linked to the load cells and attached to the loading frame. As anticipated, the inboard skin was aluminum alloy, the core skin was a honeycomb, and the FML outboard skin was aluminum alloy 2024-T3 and unidirectional glass/epoxy (FM 94-27%–S2 Glass 187–460) oriented in a cross-ply configuration. Three different FML LE structures were designed

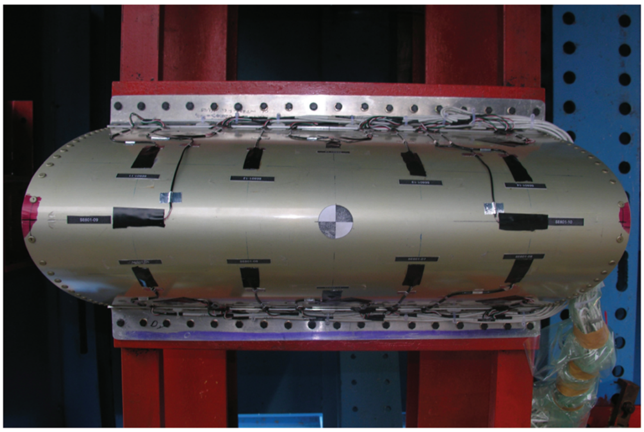

Fig. 1 The structure of support for the test article, including the location of the load cells.

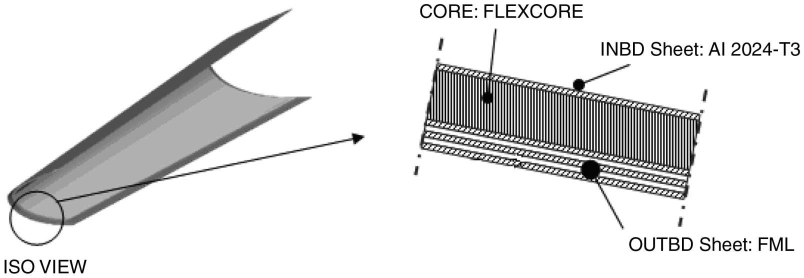

Fig. 2 Test specimen configuration (ISO represents the International Organization for Standardization).

using advanced FE simulations. They were manufactured and finally tested to analyze their impact-energy-absorbing capabilities. Three different layups of the test article were prepared, their only differences being the thicknesses of the outboard plies. The dimensions of the LE bay were the same for all of the configurations and they measured 640 × 310 mm. The layup is shown in Fig. 2. The three different configurations (see Table 1) consisted of

1) Configuration 2.1 presented a layup of A/0/90/A/90/0/A, in which A referred to a layer of aluminum alloy 2024-T3 with a thickness of 0.3 mm, and 0 and 90 referred to layers of unidirectional glass/epoxy (FM 94-27%–S2 Glass 187–460) oriented in a cross-ply configuration; each glass layer had a thickness of 0.125 mm, giving a total specimen thickness of 1.4 mm. The total weight was 1.97 kg (including the outboard, the inboard, and the core skins).

2) Configuration 2.2 presented a layup of A/0/90/A, in which the layer of aluminum had a thickness of 0.4 mm, giving a total specimen thickness of 1.05 mm. The total weight was 1.64 kg.

3) Configuration 2.3 presented a layup of A/0/90/A, in which the layer of aluminum had a thickness of 0.3 mm, giving a total specimen thickness of 0.85 mm. The total weight was 1.53 kg.

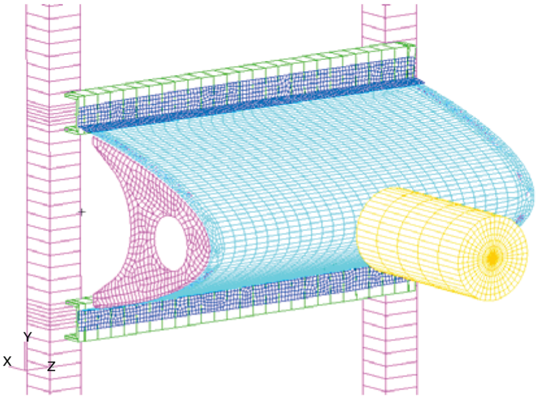

Fig. 3 FE model, including all of the composite parts.

III. Finite Element Discretization

The FE model consists of different parts (see Fig. 3): beam elements to model the fasteners and the truss; shell elements to model the ribs and the outboard and inboard skins; and a brick element used to model the honeycomb of the core layup and the bird. The two-dimensional elements (ribs, outboard and inboard plies) were modeled with four-node thin shell elements with different thicknesses. Moreover, eight-node brick elements were employed in the sandwich honeycomb core material and bird modeling. The element size was approximately 2 mm for the inboard and outboard plies and brick elements. Along the thickness of the core, the model consisted of two brick elements. All the jointed fasteners were modeled with a one-dimensional (1-D) element, and the elements used for the fittings were bar elements. The total number of FE specimens was 25.380 and 12.240 shell and brick elements, respectively; the total number of 1-D elements was 387. The element size was different for the rib elements, and it was nonuniform throughout the structure.

The 1-D elements were used to model the support frame and the two different fittings: bolts and rivets. The rivets were used to joint the rib with the skin, and the bolts were used to joint the outboard skin with the stringer of the truss.

The first type of joint was a countersunk head rivet in aluminum alloy (CSK) and the second type was a titanium Hi-Lock joint. Both fittings were modeled with a 1-D element but different properties. The material used for the rivets was aluminum alloy and the titanium material was used to model the bolts. During the FE simulations, the fracture was modeled with the Johnson–Cook criterion [12]:

$$\sigma = (A + B\varepsilon_P^n)\left(1 + C \ln \frac{\dot{\varepsilon}}{\dot{\varepsilon}_0}\right)\left[1 - \left(\frac{T - T_r}{T_m - T_r}\right)^m\right] \qquad (1)$$

where A represents the elastic limit of the material, B and n are the characteristics of the plastic hardening, and C is another constant that expresses the sensitivity to the strain rate when compared with the reference value of the strain rate $\dot{\varepsilon}_0$ fixed at 1 s^{-1}. The five parameters A, B, n, C, and m are listed in Table 2. T is the room temperature, T_{melt} is the melting temperature, and m is a constant of the material. In these tests, the T factor was not taken into account because all of the tests were performed at room temperature. Regarding the determination of the parameters A, B, C, and n in the first term of the model of Johnson–Cook, they were identified with an interpolation on a log scale graph of the experimental data obtained from tensile tests [7].

Figure 3 shows the FE model of the LE structure, the truss, and the Lagrangian bird model. The model shown in the figure contains the bird, one LE skin, two ribs, a rigid backplate, and the load frame. The load frame is divided into the interface beam and a support beam. The interface beam is used to connect the LE structure to the load frame, and they are linked to the support frame using a tied-node-to-surface-contact interface. The one-bay component is fixed along the edge on the truss, the interface structure is modeled by 1-D elements, and the LE is applied on a truss in use as a fixture with a height of 1164 mm and a width of 630 mm.

Table 1 Test specimen configuration

Configuration	Outboard, mm	Core, mm	Inboard, mm
2.1	FML $3-3/2-0.3$	Honeycomb	Al, 0.4
2.2	FML $3-2/1-0.4$	Honeycomb	Al, 0.4
2.3	FML $4-2/1-0.3$	Honeycomb	Al, 0.4

Table 2 Parameter characterization of the joints

Joint	Yield stress, A, MPa	Plastic hardening		Strain hardening, C
		B, MPa	n	
CSK	457	417	0.5	0.074
Hi-Lock	896	656	0.5	0.0128

IV. Material Properties

This section refers to the material types used to model the distinct parts of the LE. A lot of different types of material models were used from the library of the MSC.Dytran code in the development of the FE analysis [10]: the DYMAT26 orthotropic crushable material model, the MAT8A orthotropic material model, and the DMATEP isotropic elastic–plastic model.

A. Honeycomb

The energy absorption capability of an exposed crashworthy element or system is greatly affected by its structural design. The sandwich structure consists of a honeycomb core between two face plates. The significant mechanisms of energy absorption of these structures are the localized crushing of the core and the bending and stretching of the facings, although energy may be effectively absorbed through both local crushing and global deflection of the structural element as a whole. For the honeycomb core material modeling, the orthotropic crushable material model is used, for which the corresponding experimental stress–strain curve under the edgewise compression (required as input parameters) is shown in Fig. 4 and the properties are as follows: E for the fully compacted material is 0.9 GPa, the maximum τ_L is 0.8 MPa, the maximum τ_W is 1 MPa, the in-plane shear modulus of G13 is 90, and the in-plane shear modulus of G23 is 220 MPa. The input required for the material consists of two parts: data for the fully compacted state and data for the crushing behavior. For the fully compacted material, the input consists of the density, the elastic modulus, Poisson's ratio, the yield stress, and the relative volume at which the material is fully compacted. The behavior during crushing is orthotropic and characterized by uncoupled strain behavior when the initial Poisson's ratios are not supplied. During crushing, the elastic modules vary from their initial values to the fully compacted values. This variation is linear with relative volume. When the material is fully compacted, the behavior is elastic–perfectly-plastic with isotropic plasticity. The load tables define the magnitude of the average stress in a given direction as the material's relative volume changes. When defining the curves, care should be taken that the extrapolated values do not lead to negative yield stresses.

The stress–strain curve has three distinct regions: the first part of the curve is characterized from a predominant contribution to the elastic strain that comes from the vertical compression. The elastic region is characterized by the effective Young's modulus of the material; that is, the Young's modulus of a uniform material that for the same imposed stresses gives rise to the same strains. This is found by taking the slope of the unloading curve, which helps to reduce the effects of any local plastic flow. The second part of the graph shows that the aluminum honeycomb will start to plastically deform if the stress in the faces, or anywhere, exceeds the flow stress σ_y of the aluminum cell wall. The yielding behavior starts when the maximum stress in each face reaches the flow stress σ_y of the material making up the cell walls, that is given by

$$\sigma = \frac{4}{9}\left(\frac{t}{l}\right)^2 \sigma_y \tag{2}$$

If the cells deform uniformly, then the strain at which this occurs ε_D is given by

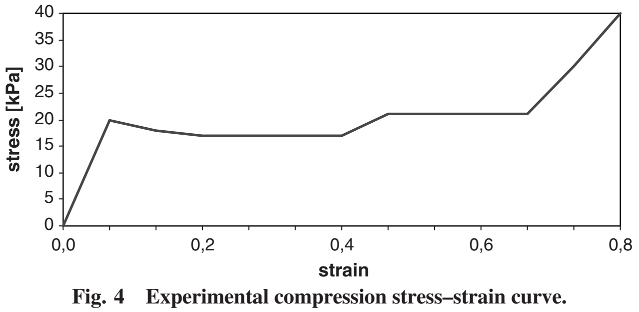

Fig. 4 Experimental compression stress–strain curve.

$$\varepsilon_D = \ell n\left(\frac{l}{l + 2l\sin\theta}\right) = \ell n\left(\frac{1}{1 + 2\sin\theta}\right) \tag{3}$$

where 90 deg $+\theta$ is the angle produced by two walls of the cells. Note, true strain is used because the strains are large and compressive. Further increases in strain cause opposing cell walls to be pressed against one another, and the stress required for further deformation increases rapidly. This continues up to a strain asymptotically equal to 0.7, at which point the stress starts to rise much more rapidly as the faces from opposite sides of the cells are pressed up against one another.

B. Fiber Metal Laminate

The outboard material is a FML, which presents as a composite material. In this way, for the FML composite face plates, the orthotropic material model is used in the shell elements to build a multilayered composite element and a classical lamination theory process, assuming that the composite ply behaves like a shell when the thickness is relatively small as compared with the other two characteristic lengths. The material describes the elastic behavior of brittle material with failure based on the interactive stress criteria of failure per mode. It includes the effects of directionality in the material stress–strain response, allowing a different fiber orientation to be specified at each through-thickness integration point for shell elements. Unidirectional laminated fiber composite shell thickness, unidirectional layer (lamina) fiber orientation, and unidirectional layer constitutive constants are required as input by the user.

The elastic stress–strain relation between the fiber and matrix stresses and strains is formulated as follows:

$$\begin{bmatrix} \sigma_{11} \\ \sigma_{22} \end{bmatrix} = \frac{1}{1 - \nu_{12}\nu_{21}} \begin{bmatrix} E_{11} & \nu_{21}E_{11} \\ \nu_{21}E_{11} & E_{22} \end{bmatrix} \begin{bmatrix} \varepsilon_1 \\ \varepsilon_2 \end{bmatrix} \tag{4}$$

and evaluated at $t + \frac{1}{2}\Delta t$.

The shear stress–strain relation is defined as

$$\gamma_{12} = \frac{1}{G_{12}}\sigma_{12} + 3\alpha\bar{\sigma}_{12}^2\sigma_{12} \tag{5}$$

where α is an experimentally derived value. Setting α to zero reduces the elastic behavior in relation to the orthotropic Hooke's law. For the prediction of failure, MSC.Dytran has a variety of materials available, and the card MAT8A is built on a set of stress-based failure criteria for the fiber and matrix failure under tensile, compressive, and/or in-plane shear loading. These failure modes can be accounted for in a shell theory in which a plane stress condition is assumed, and the failure mechanisms of delamination response associated with a splaying mode of failure and debonding were not considered. For this reason, additional input data regarding lamina strength in its principal material directions is required, although the failure criteria mentioned next are formulated as ratios of applied stress to lamina strength, with multiple terms accounting for lamina in-plane stress interactions. The basis of the model is the modification made by Matzenmiller and Sackam [13] to the well-known Chang and Chang composite damage model [14]. More specifically, failure is assumed in a ply-subject-to-tensile-fiber mode whenever the following condition is true:

Fiber breakage:

$$\left(\frac{\sigma_{11}}{x_T}\right)^2 + T \geq 1 \qquad (\sigma_{11} > 0) \tag{6}$$

where X_T was fixed equal to 725 MPa. It must be noted that T is a weighting factor for the ratio of the shear stress to shear strength, taking values in the range between 0 and 1.0. When failure occurs, the material constants E_1, E_2, υ_{12}, and G_{12} are set to zero in the corresponding unidirectional layer of the composite shell element:

$$T = \left(\frac{\sigma_{12}}{S}\right)^2 \frac{1 + \frac{3}{2}\alpha G_{12}\sigma_{12}^2}{1 + \frac{3}{2}\alpha G_{12}S^2} \tag{7}$$

In the case of the compressive fiber mode, failure is assumed in a ply whenever

$$\left(\frac{\sigma_{11}}{X_c}\right)^2 \geq 1 \qquad (\sigma_{11} > 0) \tag{8}$$

where X_c was fixed equal to 725 MPa. Similar to the previous case, when failure occurs, material constants E_1, E_2, υ_{12}, and G_{12} are set to zero in the corresponding unidirectional layer of the composite shell. Finally, the matrix failure is assumed in a ply whenever

matrix cracking:

$$\left(\frac{\sigma_{22}}{Y_T}\right)^2 + T \geq 1 \qquad (\sigma_{22} > 0) \tag{9}$$

matrix compression:

$$\left(\frac{\sigma_{22}}{2S}\right)^2 + \left[\left(\frac{Y_c}{2S}\right)^2 - 1\right]\frac{\sigma_{22}}{Y_c} + T \geq 1 \qquad (\sigma_{22} < 0)$$

where Y_T and Y_C are fixed equal to 75 MPa, and S is fixed at 75 MPa. The rules on the degradation properties describe how the stress increments are related to strain increments in the various directions after failure in a particular mode has occurred; for example, in matrix compression failure, the material constants E_2 (lateral Young's modulus) and υ_{12} (Poisson's ratio) are set to zero. Finally, the model describes how the stresses are relaxed to zero after failure has occurred. The relation can start either when a particular mode has failed or when all material properties (E_1, E_2, υ_{12}, and G_{12}) are degraded to zero according to the property degradation rule. The relation always occurs in time, either in problem time units by velocity propagation or simply by time steps. This model is referred to as the postfailure degradation rule. The material properties required for this model are given as follows: E is 30.7 GPa, σ_y is 310.3 MPa, ultimate strength σ_r is 631.4 MPa, and ε_r is 0.0064 mm/mm.

C. Aluminum Alloy 2024-T3

The material law used for the aluminum layers is an isotropic elastic–plastic thin-shell model with a plasticity algorithm that includes transverse shear effects. In addition, a Johnson–Cook yield model has been considered for the basic elastic–plastic formulation to allow the cutoff of element strength at high strains. The elastic–plastic behavior was input as a law:

$$\sigma = (A + B\varepsilon_p^n)\left(1 + C\,\ell n\,\frac{\dot{\varepsilon}}{\dot{\varepsilon}_0}\right)\left[1 - \left(\frac{T - T_r}{T_m - T_r}\right)^m\right] \tag{10}$$

In this equation, the temperature effects were not taken into account. From previous work [15], similar alloys were able to supply the following data: $A = 277$ MPa, $B = 485$ MPa, $n = 0.55$, and $C = 0.015$. The Young's modulus of 2024-T3 resulted from measurements of 72.4 GPa. Finally, Shaue and Lee [16] gave the maximum strain for 2024-T3 under uniaxial tensile loading as 18%, and so this was implemented via the isotropic damage law within the code. In this law, the total element stresses at each integration point were acted upon in the following fashion:

$$\sigma = [1 - d(\varepsilon_p)\sigma_0] \tag{11}$$

where σ was the damaged full stress tensor, $d(\varepsilon_p)$ was the isotropic scalar damage function, ε_p was the plastic strain, and σ_0 was the full-stress tensor as calculated from the undamaged elastic–plastic material law.

D. Bird Modeling

In this work, the bird has been idealized as a cylindrical bullet of homogenous material [17,18]. The numerical model of the bird geometry (shape and dimensions) and material (constitutive law and equation of state) is central in a bird strike analysis when using explicit FE codes. MSC.Dytran is an explicit code, and it adopted two different FE methods to model the impact phenomena: the Lagrangian approach and the techniques based on Eulerian or the ALE approach. Recently, a lot of solvers have introduced another approach known as the SPH method. In this report, the bird is modeled as a projectile with the shape of a cylinder [19,20] and the Lagrangian approach is adopted. The Lagrangian method consists of realizing a mesh associated with particles in the material under examination; therefore, each node of the mesh follows an individual particle in motion. This approach describes the motion because with the fixed initial position, it is possible to restore a kinetic history about any point. The imposition of boundary conditions is simplified because the boundary nodes remain on the material boundary. The other side of the Lagrangian approach has to consider the large distortions [19]. In an explicit FE analysis, the time step is determined by the smallest element dimension. The severe mesh distortion causes the time step to decrease to an unacceptably low value for the calculations to continue. These excessive distortions cause failure due to volumetric strain in some elements of the modeled bird. This paper investigates the performances of Lagrangian bird models impacting a deformable target; a valid case of this example is reported in literature by Barbers et al. [21]. Even so, this paper describes an impact of a soft cylindrical projectile against a rigid plate.

The weight of the bird used in the impact testing was 3.6 kg, the density was $\rho = 950\ \mathrm{kg/m^3}$, and the projectile was shaped as a cylinder 268 mm long with a diameter of recreated 134 mm; it was solved with the MSC.Dytran explicit FE code. The FE model of the cylinder was developed using eight-node underintegrated solid elements characterized by a progressive refinement toward the impacting end (Fig. 5). Moreover, to avoid penetrations, consequent to the distortions of the Lagrangian elements during the analysis, all of the faces of the solid elements were involved with the targeting during the impact.

V. Numerical and Experimental Correlation

Three impact tests were performed on three composite LEs with different layups (see Table 1). The impact of the composite LE was simulated for a velocity of 129 m/s, with a bird mass of 8 lb. All the configurations have satisfied the strike and no penetration was present, but the configurations absorbed the kinetic energy differently due to the impact; for each configuration, three different maximum deformations were recorded. Configuration 2.2 with outboard ply in FML $2/1 - 0.4$ was characterized by a string deformation, but this test article absorbed the total impact energy; the penetration was not present, and the failure zone affected only the inboard skin. Figure 6 shows that the inboard aluminum skin presented a shear along the interface zone, among the coupling honeycomb with the inboard ply.

Correlation between the experimental tests and the numerical simulation was attempted considering a normal impact (90 deg). Contact between the bird and the structure, and possible contact between the ribs and the rigid plate, were modeled with Lagrangian–Lagrangian contact. Self-impacting contact was used to allow all elements of the structure to collide with each other. Figure 7 presents the results on the FE model; it is possible that as the stress distributions exerted on the LE by the impacting bird had a peak on the inner skin due to a great curvature by the deformation, the stress value in this zone was higher (1200 MPa) than the allowable stress of aluminum ply (380 MPa). The model reported the most critical area of the configuration, as was the experimental test. The numerical and experimental correlation has shown good results, both in terms of

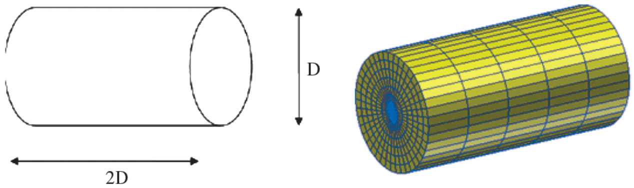

Fig. 5 FE model for a cylindrical body.

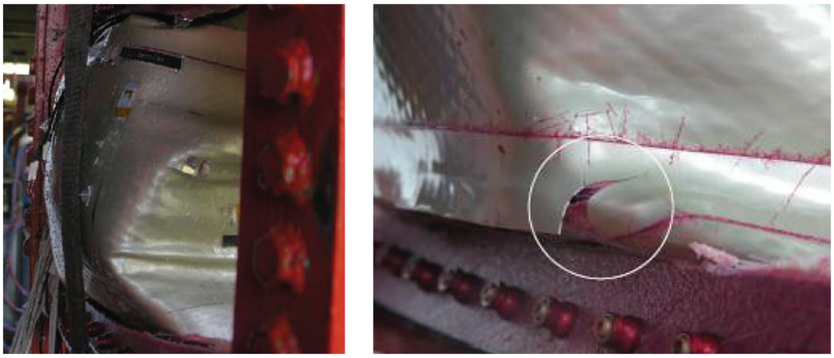

Fig. 6 Failure zone about the skin inboard for FML3 2/1 – 0.4, related to the skin inboard.

global behavior of the test article and local evolution of some measurable parameters, confirming the validity of the approach and possible guidelines for structural design including bird impact requirements.

Figure 8 shows the deformation for configuration 2.3 with outboard FML4 2/1 – 0.3, and it is visible because the zone subjected to the failure is more extended on the LE. The configuration presents the failure on both the inboard and outboard plies. This layup consists of a lower thickness for the outboard sheet than for the other two configurations (0.95 mm compare to 1.4 mm for configuration 2.1 and 1.05 mm for configuration 2.2), and these results permitted the start of a process of optimization about the thickness.

This configuration is one of the three presented larger areas damaged by the impact, and damages were on both the internal and external plies. The numerical analysis shows the area in which the maximum stress was located as the edges of the FML skin were subjected to strong deformations. Figure 9 shows the FE model was able to describe the zones with higher stress value; the numerical test presented a stress peak on the outer of 1280 MPa than the allowable stress of the FML that was 631.4 MPa.

Configuration 2.1 of the three was the one that answers to the impact, because there were no areas with visible damage and the deformation was lower than the two previous cases. This configuration presented a strong deformation, but no penetration was visible; the failure zones regarded a portion of bay larger than the two configurations, but the deformation was lower. This was due to a larger portion of the structure that was involved to absorb the impact.

The layup of the three configurations was chosen to allow an operation of refinement and optimization. The purpose of the research activity was to identify the parameters that allowed optimal weight and performance, for which reason the choice of the configuration that best satisfied these requirements was the most credited for the development of a full-scale LE, which meets the requirement of bird strike.

Figure 10 plots the numerical time histories related to the displacements of the central node for all configurations. Configuration 2.1 (FML3 3/2 – 0.3) and configuration 2.2 (FML3 2/1 – 0.4) presented a plateau, and the deformation was growing

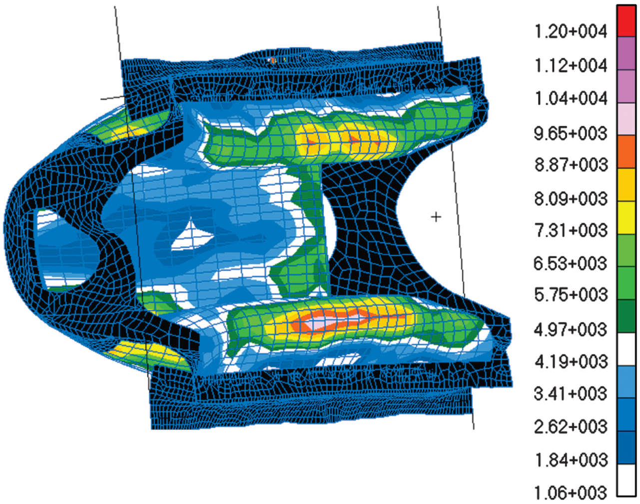

Fig. 7 Stress on the FE model in the final state of FML3 2/1 – 0.4.

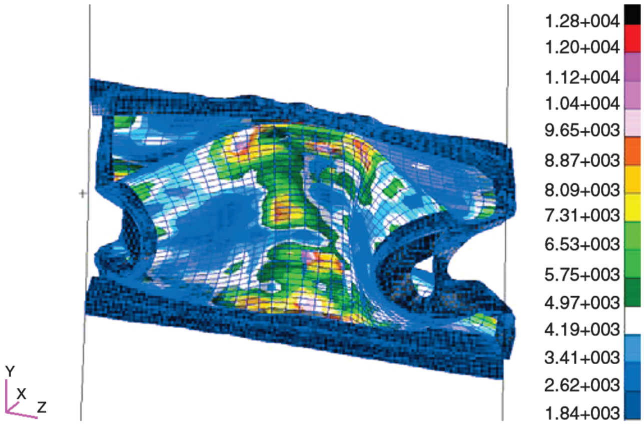

Fig. 9 Stress on the FE model in the final state of FML 2/1.

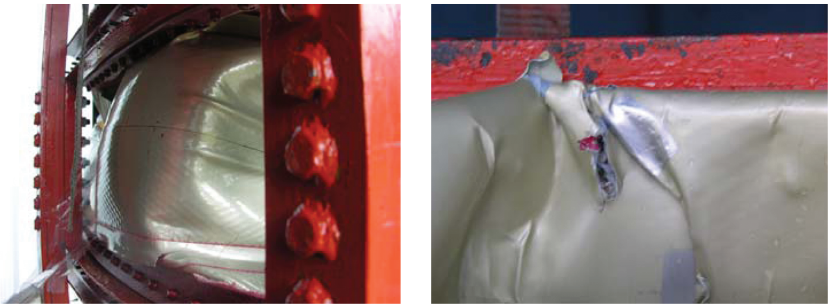

Fig. 8 Deformation about the skin inboard (left) and outboard (right) for FML3 2/1 – 0.3 configuration.

according to the dynamic impact; successively, the curve reached a stabilized line. Configuration 2.1 offered the minimum deformation of the central node. Configuration 2.3 (FML4 $2/1 - 0.3$) presented the damages, which were distributed in different parts of the bay (see Fig. 9), particularly in the central zone, so that in the time history there was an interrupt along the curve because of the failure criteria; as soon as the maximum strain was reached, the failed element disappeared and it was not considered in the analysis.

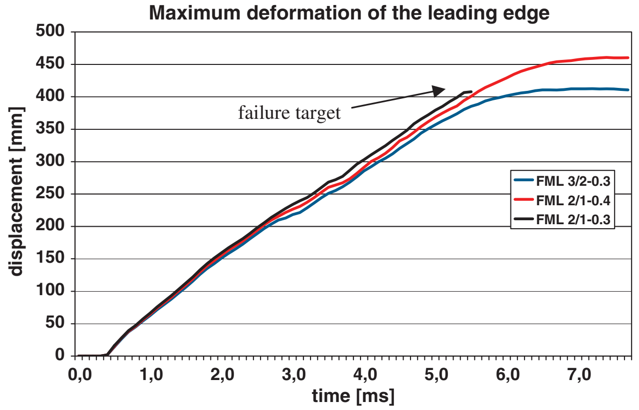

Fig. 10 Time history of the central node as related to the configurations.

Figure 11 shows the time histories for the energy absorbed by the honeycomb material for all configurations; it is possible to distinguish that the configuration with the highest outboard skin thickness absorbed more energy.

During the first phase of the impact, the absorbed energy had the same shape, successively; the trend results were different due to a major deformation of the external skin. It can be seen that configuration 2.1 (FML3 $3/2 - 0.3$) offered the maximum energy value absorbed from the honeycomb, configuration 2.2 (FML3 $2/1 - 0.4$) with the aluminum ply of 0.4 mm presented an absorbed energy value lower during the impact dynamic, and configuration 2.3 (FML4 $2/1 - 0.3$) with the aluminum ply of 0.3 mm presented a failure zone so that there was an interrupt along the curve.

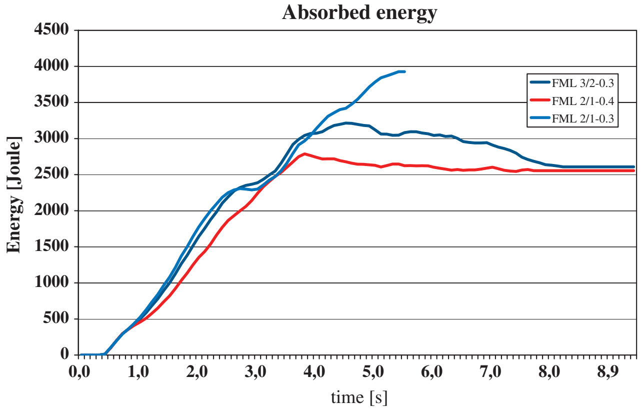

Fig. 11 Time history of the absorbed energy from the honeycomb.

In general, the FML shows a higher resistance to cracking than the nonclad 2024-T3 in a standard drop weight setup [20] or a gas gun [11]. This impact performance of FML is attributed to a favorable high-strain rate strengthening phenomenon that occurs in the glass fibers, combined with their relatively high failure strain. In particular, these results underline the behavior about the FML; configuration 2.1 (FML 3 $3/2 - 0.3$) shows more advantages related to configuration 2.2 (FML3 $2/1 - 0.4$) and configuration 2.3 (FML4 $2/1 - 0.3$) relative to the bird impact. The FML $3/2$ presents a major number of aluminum plies related to the FML $2/1$; this is favorable to absorb a major aliquot of the energy due to the impact and, in this way, produce a deformation lower than FML $2/1$. Moreover, the FML offers a 15–30% weight savings over aluminum, due to the low density. During the tests, two cameras are placed to record the events of the bird strikes: the first camera records the impact in the lateral

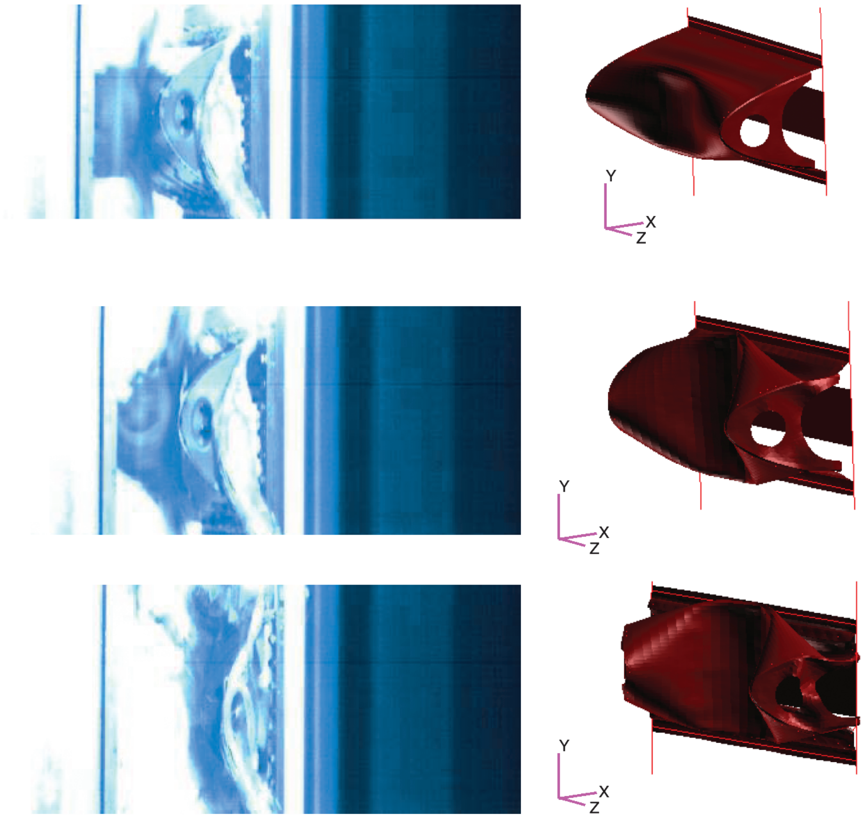

Fig. 12 Comparison between the experimental and numerical deformations after 2, 3, and 3.6 ms.

Table 3 Comparisons among three different configurations

Configuration	Weight, kg	Outboard th, mm	Numerical deformation, mm	Experimental deformation, mm	Error, %
2.1	1.97	1.4	320	305	4.6
2.2	1.64	1.05	440	420	4.5
2.3	1.53	0.85	460	434	5,6

Table 4 Numerical and experimental correlation among the reaction loads in impact direction

Configuration	Numerical loads, daN	Experimental loads, daN	Error, %
2.1	3402	3233	4.9
2.2	2585	2448	5.3
2.3	4293	4040	5.8

view at 90 deg and the second camera is dedicated to record the impact from an angle of approximately 45 deg. Figure 12 presents the correlation at increasing time intervals. The LE deformation captured by the side high-speed camera is compared to the simulation at different time intervals. In the experimental test, the LE deformation is not a visible cause of bird deformation but, from the picture, it can seen that the model provided excellent agreement with experimental data.

Table 3 presents a comparison between the configurations used in this work and the error between the numerical and experimental tests about the maximum deformations of the bay.

The experimental deformations were obtained from a graphic construction stored by a camera placed laterally to record the event. The error was lower than 5%, which was considered acceptable.

From the load cells assembled on the fixture, it was possible to correlate the reaction loads with those predicted by the FE model. An example of the time history is shown in Fig. 13, in which it can be seen that the model predicted the shape and peak magnitudes of the reaction loads reasonably well. The time histories are related to the loads recorded along the impact direction; the correlation was made in a time step in proximity of the maximum peak recorded during the test with configuration FML3 $3/2-0.3$. For the remaining two configurations, the model continued to provide excellent agreement with the experimental data.

Table 4 reported the differences between the peak magnitudes of the predicted reaction loads, and this measured in the tests, ensuring the simulations remained conservative.

VI. Conclusions

This paper has collected the results of a research program jointly developed by an industry and a university on the problem of the bird impact modeling on airplane surfaces. Several tests on a one-bay typical LE structure have been carried out, using a different layup of FML skin, and the results have been used for the numerical correlation. An explicit FE model has been developed for the impact on a LE structure with a soft projectile, using the MSC.Dytran code and according to the Lagrangian approach. The impact dynamics and penetration threshold were observed in the experiments and numerical simulations. The numerical and experimental correlation phase was the most critical aspect of such highly nonlinear behavior events, due to several uncertainties that could affect the test and the model. In general, the model was accurate to predict the final deformed shape of the LE and the absence of foreign object penetration, showing that the designed LE made with FML material was able to protect the inner LE structure from damage and satisfy certification requirements. In particular, the FML $3/2$ presented a higher resistance to the impact compared to the FML $2/1$. This performance of FML $3/2$ was attributed to a higher number of aluminum plies than the FML $2/1$, resulting in an increased value of the absorbed energy and a reduced deformation when compared with the FML $2/1$.

The application of the bird strike certification methodology, validated and verified through the test program, describes the possibility of identifying the layup that best optimizes the ratio weight/performance-to-bird-strike requirement for the types of materials that we chose. The aim of this activity is to extend the best configuration on the LE in full scale because Alenia Aeronautica is responsible for the design, manufacture, and certification of all of the LEs for the C27J airplane, and this safety-critical structure must also

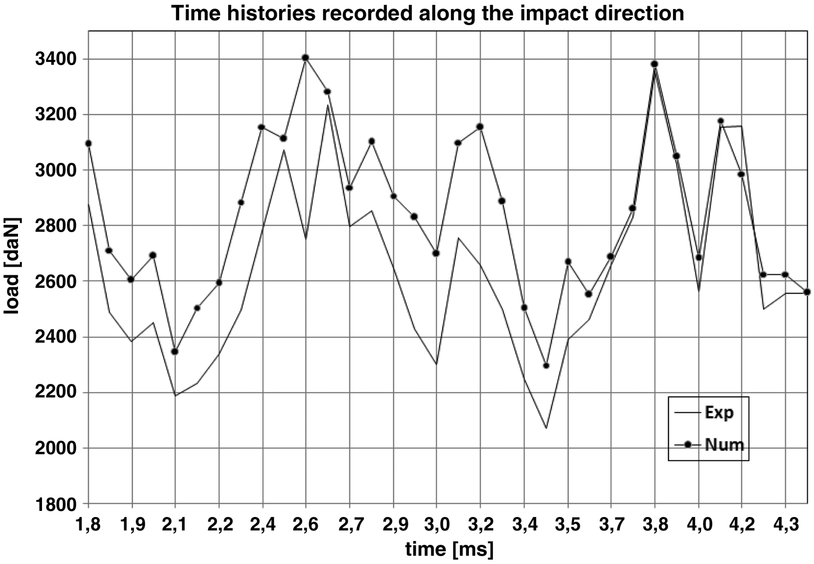

Fig. 13 Comparison between the experimental and numerical loads.

be designed according to FAA and EASA sections 25.631 [1,2] on bird strike requirements.

References

[1] "Bird Strike Damage," European Aviation Safety Agency, Certification Specifications for Large Aeroplanes, CS 25.631, Colonia, Germany, 2003.

[2] "Bird Strike Damage," Part 25 Airworthiness Standards: Transport Category Airplanes, Federal Aviation Administration, Dept. of Transportation, Sec. 25.631, Washington, D.C., 2003.

[3] "Damage Tolerance and Fatigue Evaluation of Structure," Part 25 Airworthiness Standards: Transport Category Airplanes, Federal Aviation Administration, Dept. of Transportation, Sec. 25.335, Washington, D.C., 2003

[4] Design Airspeeds," Part 25 Airworthiness Standards: Transport Category Airplanes, Federal Aviation Administration, Dept. of Transportation, Sec. 25.57, Washington, D.C., 2003

[5] Guida, M., Marulo, F., Meo, M., and Riccio, M., "Analysis of Bird Impact on a Composite Tailplane Leading Edge," *Applied Composite Materials Journal*, Vol. 15, Nos. 4–6, 2008, pp. 241–257. doi:10.1007/s10443-008-9070-6

[6] Guida, M., Marulo, F., Meo, M., and Riccio, M., "Evaluation and Validation of Multi-Physics FE Methods to Simulate Bird Strike on a Wing Leading Edge," *Proceedings of the 13th European Conference on Composite Materials* [CD-ROM], 2008.

[7] Guida, M., Marulo, F., Meo, M., Riccio, M., and Russo, S., "Analysis of Bird Strike on a Wing Leading Edge Made of Fibre Metal Laminates," *Proceedings of the 6th International Conference on Composite Science and Technology (ICCST/6)* [CD-ROM], 2007.

[8] Vogelesang, L. B., and Vlot, A., "Development of Fiber Metal Laminates for Advanced Aerospace Structures," *Journal of Materials Processing Technology*, Vol. 103, 2000, pp. 1–5. doi:10.1016/S0924-0136(00)00411-8

[9] Tsartaris, N., Dolce, F., Polimeno, U., Meo, M., Guida, M., Marulo, F., and Riccio, M., "Low Velocity Impact Behavior of Fibre Metal Laminates," *7th International Conference on Composite Science and Technology (ICCST/7)* [CD-ROM], Paper 27165, Jan. 2009.

[10] MSC.Dytran FE Code, Ver. 2005, MSC Software, Santa Ana, CA, 2005.

[11] Read, C. J., "Standard Test Method for Bird Impact Testing of Aerospace Transparent Enclosures" ASTM International, Standard F330-89, West Conshohocken, PA, 2004.

[12] Johnson, G. R., and Cook, W. H., "Fracture Characteristic of Three Metals Subjected to Various Strains, Strain Rates, Temperatures and Pressures," *Engineering Fracture Mechanics*, Vol. 21, 1985, pp. 31–48. doi:10.1016/0013-7944(85)90052-9

[13] Matzenmiller, A., and Sackam, J. L., "On Damage Induced Anisotropy for Fiber Composites," *International Journal of Damage Mechanics*, Vol. 3, 1994, pp. 71–86. doi:10.1177/105678959400300104

[14] Paris. F., "A Study of Failure Criteria of Fibrous Composite Materials," NASA, CR-2001-210661, 2005.

[15] Guida, M., "Study, Design and Testing of Structural Configurations for the Bird-Strike Compliance of Aeronautical Components," Ph.D. Dissertation, Aerospace Engineering Dept., Univ. of Naples "Federico II," Naples, Italy, 2008.

[16] Shaue, G. H., and Lee, H., "The Thermomechanical Behavior for Aluminum Alloy Under Uniaxial Tensile," *Materials Science and Engineering*, Vol. 268, 1999, pp. 154–164. doi:10.1016/S0921-5093(99)00069-6

[17] Wilbeck, J. S., "Impact Behavior of Low Strength Projectiles," Ph.D. Dissertation, Texas A&M Univ., College Station, TX, 1977.

[18] Wilbeck, J. S., "Impact Behavior of Low Strength Projectiles," Air Force Materials Lab, AFML-TR-77-134, July 1978.

[19] Airoldi, A., and Cacchione, B., "Modeling of Impact Forces and Pressures in Lagrangian Bird Strike Analyses," *International Journal of Impact Engineering*, Vol. 32, 2006, pp. 1651–1677. doi:10.1016/j.ijimpeng.2005.04.011

[20] McCarthy, M. A., Xiao, J. R., McCarthy, C. T., Kamoulakos, A., Ramos, J., Galard, J. P., and Melito, V., "Modelling of Bird Strike on an Aircraft Wing Leading Edge Made from Fibre Metal Laminates - Part 2: Modelling of Impact with SPH Bird Model," *Applied Composite Materials*, Vol. 11, No. 5, 2004, pp. 317–340.

[21] Barbers, J. P., Taylor, R., and Wilbeck, J. S., "Characterization of Bird Impacts on a Rigid Plate," U.S. Air Force Flight Dynamics Lab, TR-75-5, 1975.